BENTHAM SCIENCE

CrossMark

Current Medical Imaging

Content list available at: https://benthamscience.com/journals/cmir

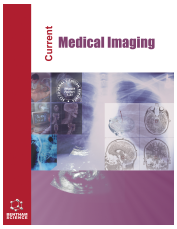

RESEARCH ARTICLE

7 Tesla MRI Liver Fat Quantification in Mice: Data Quality Assessment

Stefan Polei[1,*], Tobias Lindner[2], Kerstin Abshagen[3], Marie Liebig[3], Bernd J. Krause[4], Brigitte Vollmar[3] and Marc-André Weber[1]

[1]*Institute of Diagnostic and Interventional Radiology, Pediatric Radiology and Neuroradiology, University Medical Center Rostock, Rostock, Germany*
[2]*Core Facility Multimodal Small Animal Imaging, Rostock University Medical Center, Rostock, Germany*
[3]*Institute for Experimental Surgery, Rostock University Medical Center, Rostock, Germany*
[4]*Department of Nuclear Medicine, Rostock University Medical Center, Rostock, Germany*

Abstract:

Purpose:

The objective of this study was to evaluate the robustness of proton density fat fraction (PDFF) data determined by magnetic resonance imaging (MRI) and spectroscopy (MRS) *via* spatially resolved error estimation.

Materials and Methods:

Using standard T2* relaxation time measurement protocols, *in-vivo* and *ex-vivo* MRI data with water and fat nominally in phase or out of phase relative to each other were acquired on a 7 T small animal scanner. Based on a total of 24 different echo times, PDFF maps were calculated in a magnitude-based approach. After identification of the decisive error-prone variables, pixel-wise error estimation was performed by simple propagation of uncertainty. The method was then used to evaluate PDFF data acquired for an explanted mouse liver and an *in vivo* mouse liver measurement.

Results:

The determined error maps helped excluding measurement errors as cause of unexpected local PDFF variations in the explanted liver. For *in vivo* measurements, severe error maps gave rise to doubts in the acquired PDFF maps and triggered an in-depth analysis of possible causes, yielding abdominal movement or bladder filling as *in vivo* occurring reasons for the increased errors.

Conclusion:

The combination of pixel-wise acquisition of PDFF data and the corresponding error maps allows for a more specific, spatially resolved evaluation of the PDFF value reliability.

Keywords: MRI, Small animal, Liver fat quantification, PDFF, Data quality, NAFLD.

Article History	Received: June 19, 2023	Revised: October 06, 2023	Accepted: October 16, 2023

1. INTRODUCTION

Unbalanced nutrition is a key factor in the development of a poor state of health [1 - 3]. Especially high uptake of saturated fat may lead to severe consequences like a partial or complete occlusion of coronary vessels [4, 5] or the development of a non-alcoholic fatty liver disease (NAFLD) [6]. In this context, quantification of the organ-specific fat content is of extreme importance for an understanding, rating, and treatment monitoring of steatosis-related diseases like NAFLD [7, 8]. Based on a separation of water and fat signals by careful selection of echo times, MRI imaging provides non-invasive *in vivo* access to the local fat content. By now, these MRI-based measurements have evolved to a sophisticated method for the determination of the proton density fat fraction (PDFF), a quantitative measure for tissue triglyceride content of, *e.g.*, the

* Address correspondence to this author at the Institute of Diagnostic and Interventional Radiology, Pediatric Radiology and Neuroradiology, University Medical Center Rostock, Rostock, Germany;
E-mail: stefan.polei@med.uni-rostock.de

liver [8 - 11].

Since the complexity of the method and the data post-processing includes many potential sources of error, multiple investigations have been performed addressing the reproducibility and accuracy of PDFF measurements [12 - 14]. Especially confounding factors like the complex multipeak spectral composition of fat [15], T1 dependency [16], T2* decay [17], phase errors [18] and signal-to-noise ratio (SNR) dependence [19, 20] need to be considered. In particular, at higher field strengths (> 3 T), this is of great importance since the accuracy of PDFF may be degraded due to an enhancing effect of the elevated B0 field on, for instance, phase errors [21]. To deal with these problems, an appropriate experimental design and careful handling of the measurement parameter space is the common practice described in the literature. Although this approach has proven to provide reproducible and reliable data in general, it bears the flaw that it relies on the assumption that PDFF maps are stripped of all major confounding factors. However, local variations of the SNR or the T2* relaxation time due to abrupt tissue composition changes or foreign objects may lead to locally incorrect PDFF values without notice. In that respect, a pixel-wise measure for the reliability of the computed PDFF would be extremely advantageous. In this study, we thus have set out to demonstrate that the computation of a simple error map, based on uncertainty propagation of PDFF fitting errors, helps evaluate the robustness of the determined fat fraction for every post-processed pixel.

2. MATERIALS AND METHODS

2.1. MR Acquisition

All data were acquired on a 7 T Bruker BioSpec 70/30 system (Bruker, Ettlingen, Germany). The setup was equipped with the B-GA12S gradient inset (max. amplitude: 440 mT/m, max. slew rate: 3440 T/m/s) and a combination of a 1H transmit volume resonator (inner diameter: 86mm, T12053V3, Bruker, Ettlingen, Germany) and a 1H receive-only surface coil (2x2 Array, T11483V3, Bruker, Ettlingen, Germany). Using a standard RARE (Rapid Acquisition with Relaxation Enhancement) sequence, T2-weighted images in coronal direction were acquired for anatomical reference. The *ex vivo* data acquisition was performed with the following parameter set: TE/TR: 41 ms/2162 ms, FOV: 70 mm x 29 mm, matrix size: 460x192, slice thickness: 0.7 mm, rare factor: 8. For *in vivo* measurements parameters were: TE/TR: 41 ms/3000 ms, FOV: 70 mm x 26 mm, matrix size: 463 x 176, slice thickness: 1 mm, RARE factor: 8. Subsequently, B0-maps were taken to allow for compensation of field-inhomogeneities by shimming up to the second order. As a source for images with different phase relations between water and fat, generated raw data (intensity maps) of a standard vendor-provided T2* relaxation time measurement (6 different echo times) protocol were used. By increasing the bandwidth to 750 kHz, echo times down to 1.47 ms (fat and water out of phase) were realized. For echo spacing between the 6 subsequent echos of a single T2* measurement protocol, times of just below 1 ms were reached. Since the resonance frequency difference between the hydrogen protons of water and fat at 7 T is approximately 1 kHz, TE differences of 1 ms are not enough to sample the in and out-of-phase transition (Nyquist's sampling theorem [22]). To achieve shorter echo time (TE) intervals, four relaxation time measurement sequences with starting echoes at 1.47 ms, 1.67 ms, 1.96 ms and 2.16 ms were sequentially run and combined in post-processing. Due to this slight variation of starting echo times, the combination of all four T2* measurement raw data results in 24 echo times, with an effective echo separation of approximately 200 µs. By this approach, we are able to effectively bypass gradient switching limitations. The remaining parameters for the relaxation time measurements were: TR: 182 ms, resolution: (350 x 350 x 1000) μm^3, flip angle: 10° for *in vivo* and TR: 146 ms, resolution: (400 x 400 x 900) μm^3, flip angle: 10° for *ex vivo* measurements. Note that flip angle and repetition time were adjusted to reduce T1 bias but still achieve a reasonable signal-to-noise ratio. Spectroscopic data for evaluation of fat composition were measured *in vivo* in the liver using the stimulated echo acquisition method (STEAM) in an approximately (2.5 x 2.5 x 2.5) mm^3 large voxel positioned in the area of the right lateral lobe with the following sequence parameters: TE/TR: 3/2500 ms, averages: 128. For suppression of the water signal, the variable pulse power and optimized relaxation delays (VAPOR) [23] scheme was used.

2.2. Post-processing

To characterize the composition of the 1H MRS-derived fat spectrum of the liver, the 7 dominant peaks of the spectrum (*in vivo*) were fitted by simple Gauss pulses as shown in Fig. (**1**). From the fit results, peak positions and areas under the curve of the 6 dominant fat peaks were obtained (red arrows in Fig. **1**). The blue arrow indicates a remnant of the incompletely suppressed water peak.

For the computation of PDFF maps, MRI magnitude data were processed using a homemade script within the Igor Pro software package (V. 6.37, WaveMetrics Inc, Lake Oswego, Oregon, USA). The routine included a correction for the spectral complexity of the MRS fat spectrum and the T2* decay of both water (T2*w) and fat (T2*f). To obtain robust starting values for the pixel-wise fits, data were fitted in advance by a simple exponential decay (y=A*exp(-x/TAU)). The obtained decay constant TAU was then used as a starting value for T2*w and T2*f, and the value of the prefactor A was used as an estimation for the signal contribution from water hydrogen protons Mw. Subtraction of the exponential fit from the raw data yielded an estimation for the periodic echo time-dependent (in and out-of-phase, period length approximately 1 ms) signal modulation (see also Fig. **2a**). To guide the eye, data points were connected with straight lines in Fig. (**2a**). To get an average measure for this modulation and thus an estimation for the fat fraction, the mean peak-to-peak amplitude of the exponentially corrected data was computed and used as a starting value for the signal contribution from fat hydrogen protons Mf in the nonlinear fitting routine. Note that this estimation for the fat signal portion works best if the mean noise amplitude is smaller than the in- and out-of-phase modulation amplitude. Finally, the magnitude data Sn were fitted according to the signal model established by Zhong *et al*. [24].

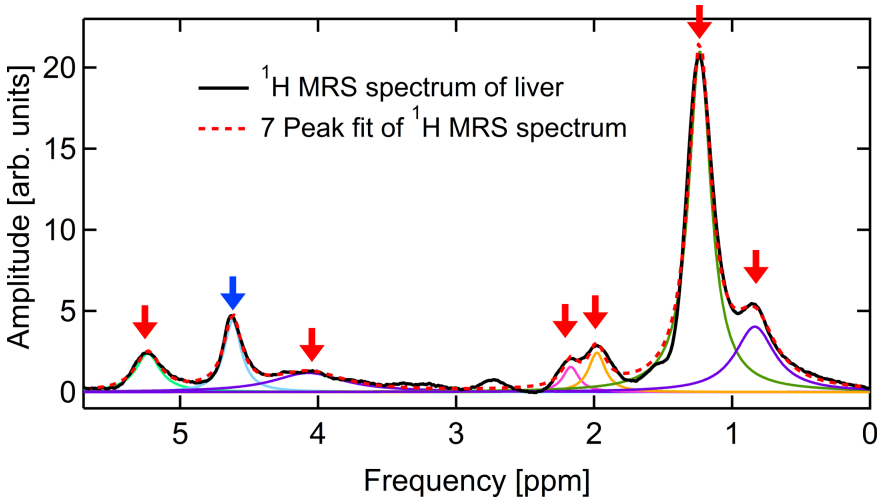

Fig. (1). *In vivo* MR liver-spectrum of a mouse suffering from NAFLD. The 7 dominant peaks were fitted by Gauss pulses (solid colored lines) to obtain peak positions and their corresponding areas. The corresponding fit is drawn in dashed red. Red arrows indicate the 6 dominant fat peaks. The blue arrow indicates a remnant of the incompletely suppressed water peak.

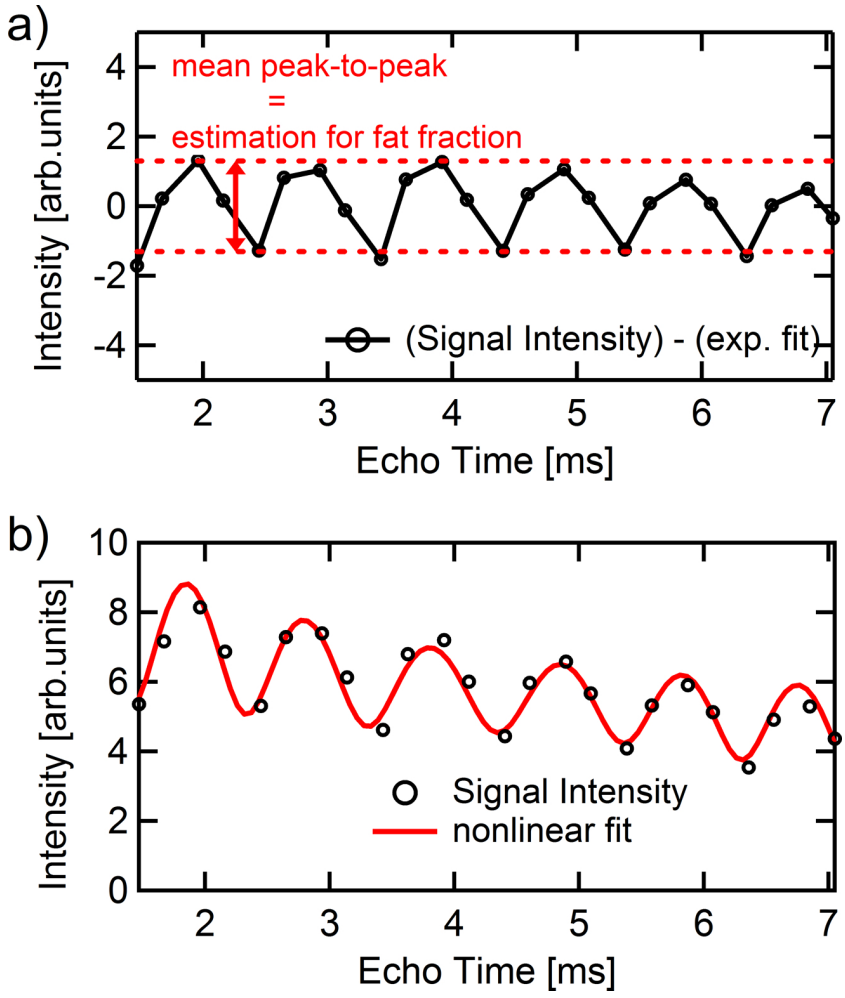

Fig. (2). Exemplary *in vivo* single pixel intensity data for different echo times. (**a**) Difference of signal intensity and exponential fit for estimation of starting values of nonlinear fit (straight lines are a guide to the eye; see text for details). (**b**) Good agreement between raw data (circles) and nonlinear fit (red solid) is evident.

$$|S_n| = \left|\left(M_w * e^{-\frac{TE_n}{T2^*_w}} + C_n M_f * e^{-\frac{TE_n}{T2^*_f}}\right)\right| \quad (1)$$

The index "n" denotes the nth echo time, and Cn is a complex, echo time-dependent coefficient representing a weighting factor for the individual MRS fat peaks (see [24] for details]. Constraining the parameter space to 0 ms-1 < 1/T2*w < 0.4 ms-1; 0 ms-1 < 1/T2*f < 0.4 ms-1; Mw, Mf > 0, biologically unlikely solutions can be avoided [24]. Using this scheme, good agreement between fit and raw data was achieved as shown in Fig. (**2b**). Once Mf and Mw are known, the fat fraction can easily be calculated according to PDFF=Mf/(Mw+Mf) for every pixel [25]. As an estimate for the robustness of the fit and thus the PDFF, the error of the PDFF (ΔPDFF) was computed according to simple quadratic propagation of error:

$$PDFF = \sqrt{\left(\frac{\partial PDFF}{\partial M_f}\Delta M_f\right)^2 + \left(\frac{\partial PDFF}{\partial M_w}\Delta M_w\right)^2} = \sqrt{\left(\frac{M_f}{(M_w+M_f)^2}\right)^2 \Delta M_w + \left(\frac{M_w}{(M_w+M_f)^2}\right)^2 \Delta M_f} \quad (2)$$

The ΔMw and ΔMf are the errors of Mw and Mf according to the nonlinear fit. In detail, ΔMw and ΔMf represent the estimated standard deviations of the fitting coefficients Mf and Mw in Eq. (1), which are derived automatically by the Igor Pro software package when the measured echo time-dependent intensity data are fitted according to Eq. (1). Note that this is a very simple estimation for the error of the PDFF, since errors of T2*w, T2*f or errors of the determination of the spectral composition of fat (leading to an error of Cn) are neglected. However, this approach is viable since it has been pointed out previously [24] that the influence of T2*w- and T2*f-errors on ΔPDFF is comparatively low. Additionally, since results for the PDFF are not severely influenced by the amount of peaks used to model the MR spectrum [26], it is safe to neglect the error of the MRS fitting as well. For pixel-wise evaluation and comparison to the computed PDFF values, the corresponding error values were stored in separate 2D error maps for each slice.

2.3. *Ex Vivo* Liver PDFF

To induce progressive NAFLD, male C57BL/6 mice (Charles River, Sulzfeld, Germany) were treated by a single intraperitoneal injection of 200 µg streptozotocin (STZ; Sigma-Aldrich, St. Louis, Missouri, USA) in 10 µl of 0.1 M trisodium citrate (pH 4.5) (Merck, Darmstadt, Germany) at day two postnatal. Starting at day 28 of age, the mice were fed a continuous high-fat diet (HFD; fat content: 60 kJ%; D12492(II) modified experimental diet; Ssniff, Soest, Germany) [27]. The mice were kept on water and HFD ad libitum at a 12-hour light/dark cycle. Please note that the main focus of this study is not the streptozotocin induces NAFLD but to present an error map-based approach for data quality assessment. The liver disease associated with the animal model was used to exemplify the advantages of the error maps on a few animals. Robustness to noise and precision of the error map approach was addresses in an digital phantom study for several fat contents (see appendix). For *ex vivo* measurements, one liver explant from a 14-week-old obese mouse that had developed steatosis was used. Directly after the explanation, the left lateral liver lobe was removed, stored in 0.9% NaCl solution and measured within the next two hours.

2.4. *In Vivo* Liver Fat Quantification

For *in vivo* measurements, one 20-week-old STZ/HFD-treated mouse (steatotic/fibrotic liver with tumors) was anesthetized by a mixture of isoflurane and oxygen. During the measurements, the isoflurane proportion was adjusted to keep the respiration rate near 35 breaths per minute. For all *in vivo* measurements, respiratory gating was applied. Body temperature was kept constant at 37°C by positioning the mouse on a warm water-flushed silicon pad.

3. RESULTS

3.1. *In Vivo* Liver Fat Quantification

The fat content of two fat-water emulsion phantoms (milk products obtained from the local grocery store, indicated fat content: 10% for "cooking cream", HanSano, Upahl, Germany and 30% for "Crème fraîche", Dr. Oetker, Bielefeld, Germany) was determined from MR spectra by computing ratios of the summed area of dominant fat peaks *vs*. summed area of all fitted peaks (see also [28]) yielding a fat content of 13.0% and 28.0% for cooking cream and Crème fraîche phantom, respectively. Subsequently, mean PDFF values for both phantoms were computed to 9.4% (cooking cream) and 27.0% (Crème fraîche). Hence, good agreement between declared fat content and PDFF calculation, as well as MRS and PDFF results, is evident.

3.2. *Ex Vivo* Data Quality

A PDFF map through the middle of the liver lobe explant is shown in Fig. (**3a**). Within the lobe, a relatively homogenous distribution of the PDFF with an average value of 29% was found. Due to the lack of fat in the area outside the liver lobe, the fitting routine did not deliver reasonable data, resulting in arbitrary PDFF values. Closer examination reveals several sharply outlined, stripe-like reductions of the PDFF to values near 10% in the area marked with a green circle. Additionally, an increase of the PDFF to values > 30% in areas between some of the stripe-like reductions was observed.

In Fig. (**3b**), the corresponding error map is shown. Note the depicted relative error refers to the ratio between computed ΔPDFF (Eq. (2)) and computed PDFF (=Mf/(Mw+Mf)). Similar to the PDFF map, the error distribution was mostly homogenous, with an average value of approximately 19%. Again, a green circle marks the area where, in the corresponding PDFF map, pronounced variations are evident. However, in the relative error map, only minor deviations from the mean error were found. A comparison with the T2w anatomy data (Fig. **3c**) revealed several vessel-like features over the whole, otherwise homogeneously appearing, liver. In the area marked with the green circle, these features were particularly obvious. Note that in Fig. (**3b**), values exceeding the color scale range are given in blue.

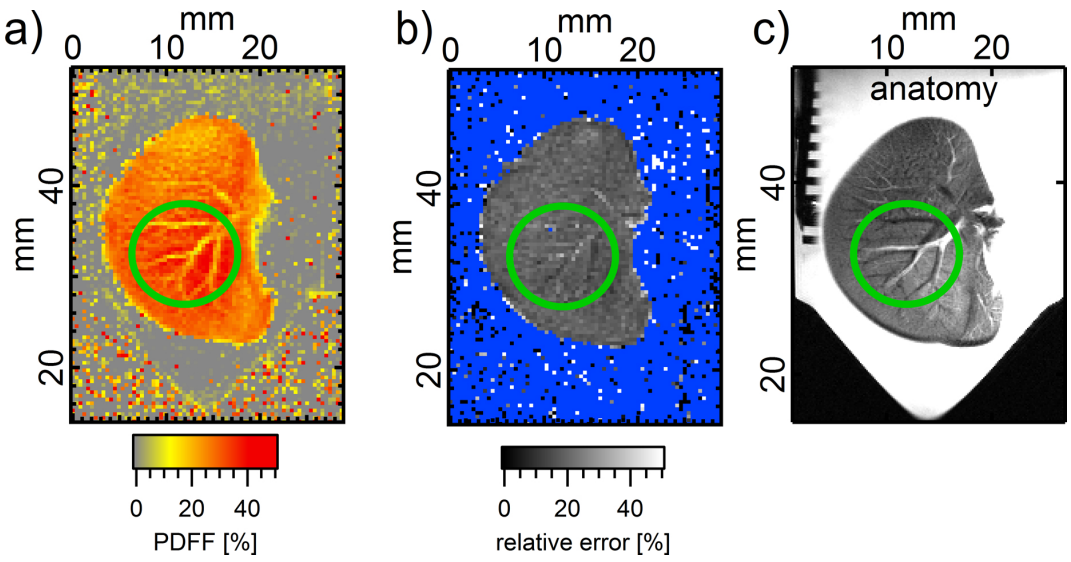

Fig. (3). PDFF, relative error and anatomy images of a liver explant (**a**): False-color representation of the PDFF of a slice through the middle of a liver lobe explant. An area of abrupt changes from the otherwise homogenous PDFF is marked by a green circle. (**b**): Corresponding relative error map of **a**). Values exceeding the color-scale range are drawn in blue. (**c**): Corresponding T2w anatomy.

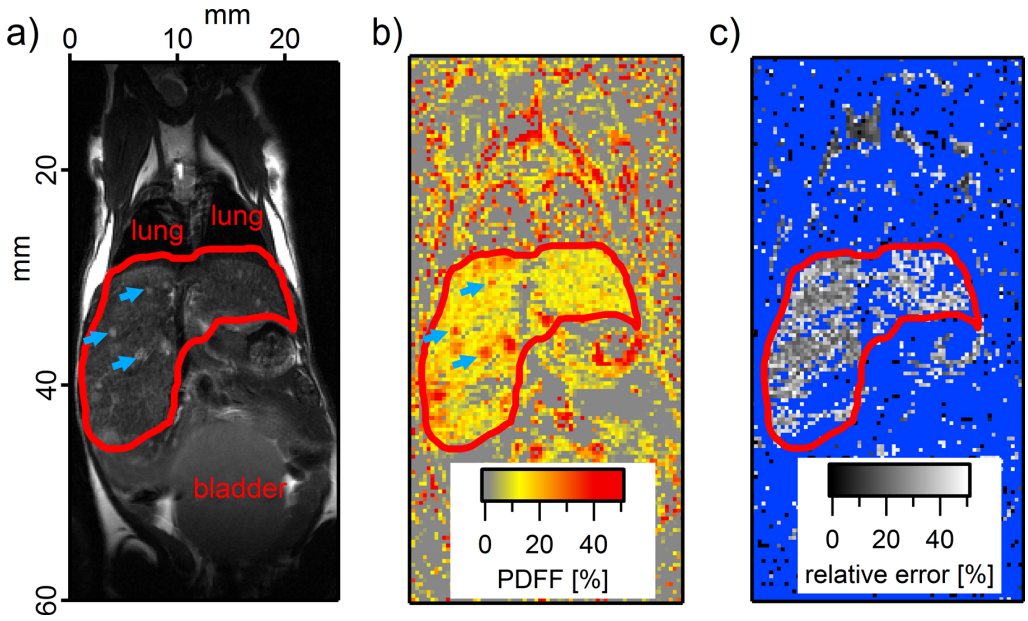

Fig. (4). *In vivo* mouse measurements. The liver is outlined in red. Blue arrows point to spots of increased intensity in T2w- and PDFF-images. (**a**): T2w coronal slice of a 20-week-old STZ/HFD-treated mouse. (**b**): PDFF map in false-colors. (**c**): Corresponding relative error map.

3.3. *In Vivo* Liver Fat Results

In vivo measurements are summarized in Fig. (**4**). In the T2w image (Fig. **4a**), a coronal slice through the mouse's trunk is shown. Below the lungs and above the bladder, the liver is marked in red. The organ did not appear homogeneous; bright spots of different sizes were found at various locations. Some were marked with blue arrows. In Fig. (**4b**), the corresponding PDFF map is depicted. The same custom-made continuous color scale as in Fig. (**3a**) was used to resemble three different fat content classes. Within the liver, large areas of medium fat content (between 10% and 25% - yellow in Fig. **4b**) were dominating. In between, small contiguous areas of low-fat content (<10% - gray in Fig. **4b**) were observed.

Additionally, small hot spots of high-fat content (>25% - red in Fig. **4b**) could be identified at various locations in the organ. Some bright spots found in the T2w image were also identified as areas of increased fat content in the PDFF map (blue arrows). The simultaneously computed relative error map of the PDFF data is shown in Fig. (**4c**). In the upper part of the liver areas, errors between 30% and 50% were found, but especially in the lower part, the relative errors were mainly above 50%.

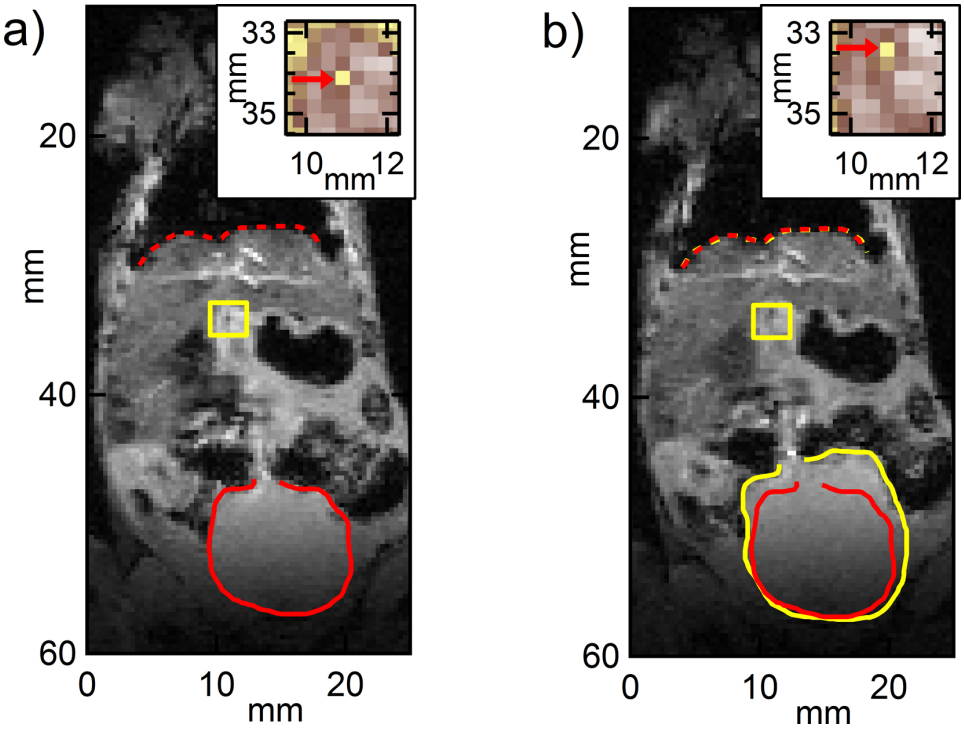

Fig. (5). MR-signal intensity maps for two different echo times. **a**) TE = 6.36 ms and **b**) TE = 7.05 ms. Bladder and diaphragm are indicated by solid and dashed red lines, respectively. The inset shows a magnification of the area marked with a yellow box. The red arrow points at a characteristic low-intensity pixel that is shifted upwards in **b**) with respect to **a**).

Triggered by unexpectedly large errors in Fig. (**4c**), the underlying raw data (intensity maps for different echo times) were analyzed as well. In Fig. (**5a**), the intensity for an echo time of 6.36 ms, taken from the 1st of the four T2* measurement sequences (see section MR Acquisition), is shown, whereas Fig. (**5b**) represents intensity data for an echo time of 7.05 ms. But this time taken from the 4th T2* measurement sequence. Since Fig. (**5**) represents the same slice position depicted in Fig. (**4**), the same anatomical features like the lung, diaphragm (indicated by dotted lines) or the bladder (indicated by solid lines) can be identified above and below the liver. Additionally, an area containing a single low-intensity pixel, surrounded by otherwise high-intensity pixels, was identified in Fig. (**5a** and **b**) and was marked with a yellow box. The image area inside the box is magnified and drawn in false colors as insets in Fig. (**5a** and **b**). It is important to note that the yellow box in both images (a) and (b) has exactly the same dimensions and is situated at the same absolute coordinates.

The diaphragm in Fig. (**5a** and **b**) was found at the same position as can be seen by the nearly perfect overlap of the red dotted line (diaphragm position at 6.36 ms) and yellow dotted line (diaphragm position at 7.05 ms) as shown in Fig. (**5b**). However, as depicted in Fig. (**5b**) the bladder at 6.36 ms (red solid) appeared much smaller than at 7.05 ms (yellow solid). Additionally, the characteristic low-intensity pixel was observed to be shifted upwards (*i.e.*, in positive y-direction) in Fig. (**5b**), when compared to Fig. (**5a**) by approximately 0.6 mm.

4. DISCUSSION

In this study, we established a method to measure the PDFF with a Bruker 7 T small animal MRI. For that purpose, echo spacing limitations of current generation gradient systems had to be overcome by an interleaved measurement approach, which combines 4 T2* measurement sequences with different starting echo times. As for the data post-processing, a simple but robust approach for the determination of starting values for the fitting routine, including T2*w, T2*f, Mf, and Mw, was established *via* exponential fitting and determination of the mean peak-peak amplitude of the intensity data after exponential subtraction.

MRI-based fat fraction determination has strong advantages over biopsy, the current gold standard for NAFLD diagnosis [29]. Besides being non-invasive, MRI PDFF measurements allow for an analysis of the whole organ, thus effectively eliminating sampling errors [30]. In addition, MRI fat fraction measurement may reduce costs and morbidity compared with biopsy [25]. However, due to its indirect nature, confounding factors and site-specific differences in MRI hardware, the method is still being put to the test with respect to accuracy and reproducibility in several studies [31 - 35]. We opted to address this issue from a different perspective: *Via* comparison to a simultaneously computed error map, the PDFF data quality can be assessed directly and, if necessary, for individual pixels.

In contrast to previous studies, where correlations between more general aspects like study conception (for instance, magnitude *vs*. complex or hybrid computation of PDFF [20]) or

global parameter influence (*e.g.*, T1 dependence [16]) on the PDFF accuracy were investigated, the error map approach presented here aims at providing a spatially resolved measure for quality assessment of PDFF data on a pixel by pixel basis. Thus, the suggested relative error map resembles an additional quality control factor that allows for the definition of, *e.g.*, an error threshold value above which PDFF data may be discarded.

Ex vivo measurements yield a mean value of 29% (PDFF) for the whole liver slice. As can be seen in Fig. (**3a**), the PDFF map of the organ appears largely homogenous. However, sudden changes in the marked region in Fig. (**3a**) are in clear contrast to the otherwise smooth appearance of the PDFF map. A comparison with the anatomic data (Fig. **3a**) strongly suggests that the stripe-like features in the PDFF map, in fact, resemble blood vessels. The hyperintense appearance of some vessels in Fig. (**3c**) is attributed to a partial filling of the same with the surrounding saline (NaCl) solution. However, such a direct comparison to anatomic data with a clear contrast between individual tissue components (here: vessel structures and liver tissue) might not always be possible. Without further investigation, it might not always be clear if unexpected PDFF changes resemble an anatomic (*e.g.*, different tissue components) or a PDFF (*e.g.*, homogeneous tissue with local fat content variation) related feature. Furthermore, ruling out the former by comparison with anatomical measurements would still leave the question open whether the sudden PDFF changes are real or are an indication of faulty post-processing. Thus, in any case, a localized assessment of the PDFF data is required.

For the explanted liver, the evaluation of the relative error map (Fig. **3b**) yields only slight increases in the relative error at positions of the sharply outlined PDFF value reductions within the green circle. In fact, such an increase of the relative error is expected for areas of reduced fat content due to the worse SNR of the measured intensity data and is in agreement with previous investigations of the noise dependency of the PDFF [16]. Thus, consistency with anatomic data and unobtrusive relative error map suggests that all features within the circle in Fig. (**3a**) represent real changes in the fat fraction.

The ability to reliably distinguish fine structures of reduced PDFF adjacent to areas of elevated PDFF may also be relevant for MR-based investigations of arteriosclerosis or similar diseases exhibiting a comparable combination of low-fat (free blood vessel) and adjacent high-fat content (fat deposits) [36].

When comparing *in vivo* T2w (Fig. **4a**) and PDFF images (Fig. **4b**), a correlation between bright spots in the anatomy (blue arrows) and high-fat content in the PDFF appears evident. A similar local accumulation of fat in the mouse liver has also been reported by Mahlke *et al*. [21] and is a characteristic feature of the late phase of NAFLD in the mouse model used [27]. For the whole lower part of the liver, errors are quite large, especially when compared to Fig. (**3b**). Despite a mostly convincing PDFF map and strong correlations to the T2w data, this puts the reliability of the *in vivo* fat content data in question. Since measurement parameters and tissue composition are similar for the *in vivo* and *ex vivo* data, another reason for the large differences between the errors of both measurements must be present. To further analyze this issue, MR raw data for two different echo times were compared in Fig. (**5**). As the cause for the high error in Fig. (**4c**), certainly, movement is definitely a probable candidate. However, breathing-related movement can be ruled out due to the constant diaphragm position, which was checked for all 24 intensity images in the same way as described above for Figs. (**5a** and **5b**). The surprising enlargement of the bladder illustrated in Fig. (**5b**) hints towards another possibility: since the measurements at 6.36 ms and 7.05 ms were part of two different T2* sequences, there is a time interval between both of several minutes. Obviously, this interval is long enough to induce either a significant filling of the bladder or an abdominal movement that causes a bladder displacement, leading to an apparent bladder enlargement. However, in either case, a compression or movement in the abdomen, including the liver, appears to be the consequence. This becomes evident when comparing the area inside the yellow box in Fig. (**5a** and **b**): The low-intensity pixel (colored yellow in the inset) serves as an indicator for the compression/movement caused by the bladder filling/displacement. Between the position of the low-intensity pixel in the insets of Fig. (**5a** and **b**), a shift vector in the y-direction of approximately 2 pixels is found, which serves as an estimate for the overall abdominal movement. Since the PDFF calculation is based on an analysis of intensity modulation of the same pixel for different echo times, a shift of that very pixel during the measurement may have severe consequences for the quality of the nonlinear fit. This is especially true for abrupt junctions between high and low-fat areas. Although the fitting routine in such a case might still converge, errors are larger than without movement. In that respect, high errors found in Fig. (**4c**) are attributed to a partial movement-related corruption of the raw data. A possible route to avoid these problems would be to either speed up the measurement, which comes at the cost of data quality (due to *e.g.* reduced resolution or reduced number of averages) or to prevent bladder filling or abdominal movement in general by for instance fasting prior to the measurement.

A limitation of this study is the limited amount of in and *ex-vivo* data available for statistical evaluation of the benefits of the error map approach. This would require a larger cohort of samples/mice/phantoms, which was beyond the scope of this work. Another point is that the dynamic range of the PDFF data obtained here is limited to values below 50% due to the chosen magnitude approach [25]. However, the magnitude fitting technique is considered to be more robust in comparison to complex fitting since the phase information is rejected [21]. In addition, a direct comparison of PDFF values to triglyceride content or histopathology was not performed, but a good correlation between the latter two and the PDFF values at 7 T in mice in a magnitude approach has been shown elsewhere [21]. Finally, the computed relative errors might be overestimated since, so far, the worsening of the SNR upon echo time increase (due to the T2* decay of the signal amplitude) is not considered. Thus, especially for the combination of low-fat content and elevated noise levels in the raw data, differences in signal amplitudes for in and out-of-phase data might drop to levels comparable to the SNR for elevated echo times. This effect might be accounted for by adding a corresponding weighting in the fitting routine.

CONCLUSION

In summary, we have presented a possible route for quality assessment of PDFF data based on comparison with simultaneously determined error maps. The benefits of the

suggested pixel-wise error analysis have been demonstrated to show their potential relevance for data quality investigations in *ex vivo* measurements and for error diagnostics for *in vivo* measurements.

LIST OF ABBREVIATIONS

MRI	=	Magnetic Resonance Imaging
MRS	=	Magnetic Resonance Spectroscopy
NAFLD	=	Non-Alcoholic Fatty Liver Disease
PDFF	=	Proton Density Fat Fraction
SNR	=	Signal to Noise Ratio
STEAM	=	Stimulated Echo Acquisition Method
VAPOR	=	Variable Pulse Power and Optimized Relaxation
STZ	=	Streptozotocin
HFD	=	High Fat Diet

ETHICS APPROVAL AND CONSENT TO PARTICIPATE

All animal experiments were approved by the State Department of Agriculture, Food Security and Fisheries Mecklenburg-Vorpommern (LALLF M-V/TSD/7221.3-1-039/14).

HUMAN AND ANIMAL RIGHTS

No humans participated in this research. The experimentation on animals was in accordance with the European Directive 2010/63/EU and, the German Animal Welfare Act (Tierschutzgesetz) and the Animal Welfare Laboratory Animal Ordinance (Tierschutz-Versuchstierverordnung).

CONSENT FOR PUBLICATION

Only animals were used in this study; hence, there is no consent for publication.

AVAILABILITY OF DATA AND MATERIALS

The data that support the findings of this study are available from the corresponding author [S.P] upon reasonable request. Data are located in controlled access data storage at Rostock University Medical Centre.

FUNDING

This work was financially supported by the Deutsche Forschungsgemeinschaft (DFG, Bonn-Bad Godesberg, Germany; grant number: AB 453/2-1) and the Europäischer Fonds für Regionale Entwicklung (EFRE).

CONFLICT OF INTEREST

The authors declare no conflict of interest, financial or otherwise.

ACKNOWLEDGEMENTS

The authors thank the Medical Faculty of the Rostock University Medical Center for the financial support of the imaging consortium and gratefully acknowledge the technical support by Romina Rauer and Anne Möller.

APPENDIX – DIGITAL PHANTOM

To generate a digital phantom, a 2D map containing areas of different percentages of fat in water was defined (see Fig. **A1**). Using this map, Eq. (1) allows for a computation of the signal intensity for different echo times. The necessary data for the determination of Cn were taken from the spectrum presented in Fig. (**1**). For T2*f and T2*w, typical values as derived from the nonlinear fitting routine for liver tissue were used: T2*w = 5 ms T2*f = 8 ms. To investigate robustness of the nonlinear fitting routine and usability of the error maps, noise with a defined standard deviation of its amplitude was generated and added to the computed raw data. To investigate the influence of noise on the output of the nonlinear fitting routine and the error map, different levels of noise with Gaussian distribution were added to simulated raw data (digital phantom). In Fig. (**A1a**), a 2D map with rectangular areas of different water/fat ratios is shown. In the background of the rectangles, fat/water ratio was varied from left to right nonlinearly from 50% to 5%. Adding noise with a standard deviation of its amplitude corresponding to 0.5% (1.5%) of the signal intensity of a "water only" phantom (in the initial state, *i.e.*, at TE = 0) to the raw data and subsequent nonlinear fitting results in PDFF and corresponding relative error (=ΔPDFF/PDFF) map shown in Fig. (**A1b** and **c**) (respectively Fig. **A1d** and **e**). Comparing Fig. (**A1a** and **b**), only for the leftmost rectangle, a slight difference between real fat content and computed PDFF is found (3.0% *vs*. 3.2%).

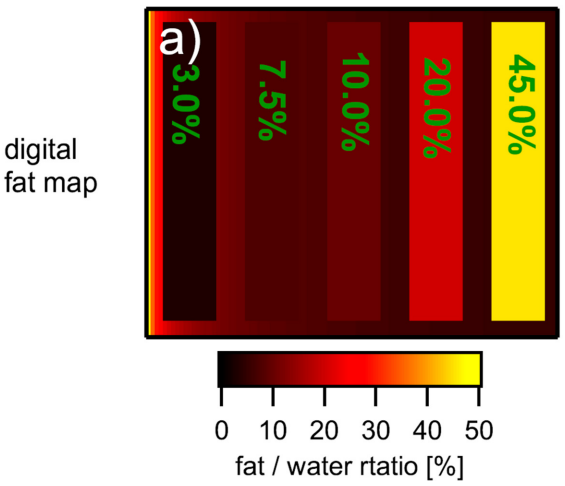

Fig. A1 contd.....

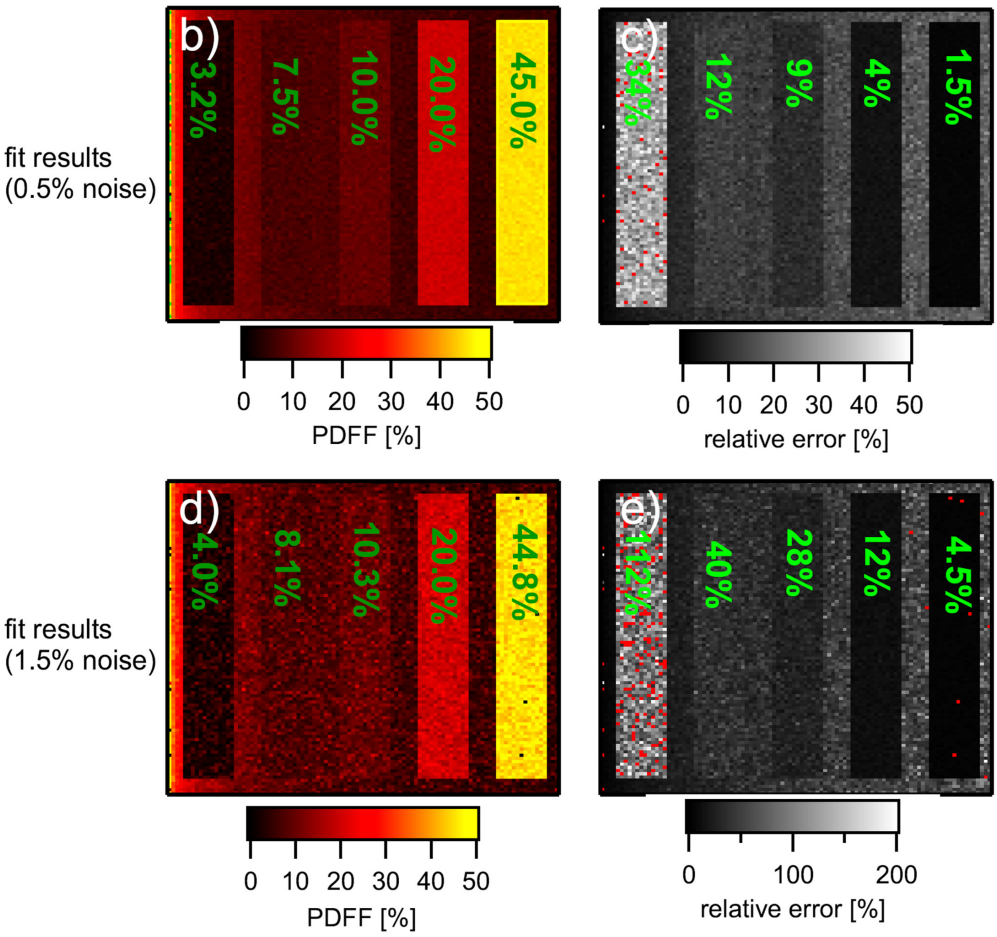

Fig. (A1). Digital phantom analysis. **a**): Digital fat/water phantom with rectangular areas of different fat percentages as indicated in green. Corresponding PDFF maps for 0.5% noise (**b**) and 1.5% noise (**d**). Simultaneously computed error maps for 0.5% and 1.5% noise are shown in **c**) and **e**), respectively, with mean errors of individual rectangles drawn in green. Red pixels in **c**) and **e**) represent errors exceeding the color scale range in the corresponding picture. MR-signal intensity maps for two different echo times.

In Fig. (**A1c**), the error map corresponding to Fig. (**A1b**) is shown. High relative errors are colored bright, and low relative errors are dark. For the highest fat content of 45% a relative error of 1.5% is evident, whereas the relative error for the lowest fat content (3.2%) is found to be higher with 34%. When the noise level is increased to 1.5%, deviations between computed PDFF and phantom become larger, especially for the lower fat contents of 3.0% and 7.5%; the routine yields higher values of 4.0% and 8.1% PDFF, respectively. Comparing Fig. (**A1d** and **e**), a similar error correlation between fat content and relative error is found for the case of 0.5% noise: inversely proportional to the fat content, relative errors increase in a non-linear way. A comparison between Fig. (**A1c** and **e**) with respect to the mean errors for the same fat fraction reveals an increase of the relative error by a factor of approx. 3, when the noise is increased from 0.5% to 1.5%. This result is expected, and it indicates that *via* the error map, a consistent estimation of the noise-related error can be achieved. Taking into account that in the raw data, a lower fat fraction is represented by the reduced amplitude of the sine-like modulation of the signal intensity with the echo time (see also Fig. **2b**), the increase of the relative error with decreasing fat fraction (see Fig. **A1c** and **e**) can directly be understood as a consequence of a reduction of the (effective) signal (*i.e*. the modulation amplitude) to noise ratio. The inverse proportionality of error and fat fraction demonstrated here is in agreement with previous investigations of noise dependency of the PDFF [16]. Due to generally higher SNR in Fig. (**A1b**) compared to Fig. (**A1d**), the effect is more pronounced for the case of 1.5% added noise.

REFERENCES

[1] Luyckx VA, Brenner BM. Birth weight, malnutrition and kidney-associated outcomes—a global concern. Nat Rev Nephrol 2015; 11(3): 135-49. [http://dx.doi.org/10.1038/nrneph.2014.251] [PMID: 25599618]

[2] Anderson AS, Key TJ, Norat T. European Code against Cancer 4th Edition: Obesity, body fatness and cancer. Cancer Epidemiol 2015; 39(S1): S34-45.

[3] Global status report on noncommunicable diseases 2014. 2014. Available from: https://www.who.int/publications/i/item/9789241564854

[4] Hu FB, Stampfer MJ, Manson JE, *et al.* Dietary saturated fats and their food sources in relation to the risk of coronary heart disease in women. Am J Clin Nutr 1999; 70(6): 1001-8. [http://dx.doi.org/10.1093/ajcn/70.6.1001] [PMID: 10584044]

[5] Kelemen LE, Kushi LH, Jacobs DR Jr, Cerhan JR. Associations of dietary protein with disease and mortality in a prospective study of postmenopausal women. Am J Epidemiol 2005; 161(3): 239-49. [http://dx.doi.org/10.1093/aje/kwi038] [PMID: 15671256]

[6] Nigro D, Menotti F, Cento AS, *et al.* Chronic administration of

saturated fats and fructose differently affect SREBP activity resulting in different modulation of Nrf2 and Nlrp3 inflammasome pathways in mice liver. J Nutr Biochem 2017; 42: 160-71.
[http://dx.doi.org/10.1016/j.jnutbio.2017.01.010] [PMID: 28189916]

[7] Than NN, Newsome PN. A concise review of non-alcoholic fatty liver disease. Atherosclerosis 2015; 239(1): 192-202.
[http://dx.doi.org/10.1016/j.atherosclerosis.2015.01.001] [PMID: 25617860]

[8] Reeder SB, Sirlin CB. Quantification of liver fat with magnetic resonance imaging. Magn Reson Imaging Clin N Am 2010; 18(3): 337-357, ix.
[http://dx.doi.org/10.1016/j.mric.2010.08.013] [PMID: 21094444]

[9] Bannas P, Kramer H, Hernando D, *et al.* Quantitative magnetic resonance imaging of hepatic steatosis: Validation in ex vivo human livers. Hepatology 2015; 62(5): 1444-55.
[http://dx.doi.org/10.1002/hep.28012] [PMID: 26224591]

[10] Simchick G, Yin A, Yin H, *et al.* Fat spectral modeling on triglyceride composition quantification using chemical shift encoded magnetic resonance imaging. Magn Reson Imaging 2018; 52: 84-93.
[http://dx.doi.org/10.1016/j.mri.2018.06.012]

[11] Ruschke S, Pokorney A, Baum T, *et al.* Measurement of vertebral bone marrow proton density fat fraction in children using quantitative water–fat MRI. MAGMA 2017; 30(5): 449-60.
[http://dx.doi.org/10.1007/s10334-017-0617-0] [PMID: 28382554]

[12] Hernando D, Sharma SD, Aliyari Ghasabeh M, *et al.* Multisite, multivendor validation of the accuracy and reproducibility of proton-density fat-fraction quantification at 1.5T and 3T using a fat-water phantom. Magn Reson Med 2017; 77(4): 1516-24.
[http://dx.doi.org/10.1002/mrm.26228] [PMID: 27080068]

[13] Meisamy S, Hines CDG, Hamilton G, *et al.* Quantification of hepatic steatosis with T1-independent, T2-corrected MR imaging with spectral modeling of fat: blinded comparison with MR spectroscopy. Radiology 2011; 258(3): 767-75.
[http://dx.doi.org/10.1148/radiol.10100708] [PMID: 21248233]

[14] Tang A, Desai A, Hamilton G, *et al.* Accuracy of MR imaging-estimated proton density fat fraction for classification of dichotomized histologic steatosis grades in nonalcoholic fatty liver disease. Radiology 2015; 274(2): 416-25.
[http://dx.doi.org/10.1148/radiol.14140754] [PMID: 25247408]

[15] Yu H, Shimakawa A, McKenzie CA, Brodsky E, Brittain JH, Reeder SB. Multiecho water-fat separation and simultaneous *R* estimation with multifrequency fat spectrum modeling. Magn Reson Med 2008; 60(5): 1122-34.
[http://dx.doi.org/10.1002/mrm.21737] [PMID: 18956464]

[16] Liu CY, McKenzie CA, Yu H, Brittain JH, Reeder SB. Fat quantification with IDEAL gradient echo imaging: Correction of bias from T_1 and noise. Magn Reson Med 2007; 58(2): 354-64.
[http://dx.doi.org/10.1002/mrm.21301] [PMID: 17654578]

[17] Hines CDG, Yu H, Shimakawa A, McKenzie CA, Brittain JH, Reeder SB. T_1 independent, T_2 * corrected MRI with accurate spectral modeling for quantification of fat: Validation in a fat-water-SPIO phantom. J Magn Reson Imaging 2009; 30(5): 1215-22.
[http://dx.doi.org/10.1002/jmri.21957] [PMID: 19856457]

[18] Yu H, Shimakawa A, McKenzie CA, *et al.* Phase and amplitude correction for multi-echo water–fat separation with bipolar acquisitions. J Magn Reson Imaging 2010; 31(5): 1264-71.
[http://dx.doi.org/10.1002/jmri.22111] [PMID: 20432366]

[19] Wen Z, Reeder SB, Pineda AR, Pelc NJ. Noise considerations of three-point water-fat separation imaging methods. Med Phys 2008; 35(8): 3597-606.
[http://dx.doi.org/10.1118/1.2952644] [PMID: 18777920]

[20] Yu H, Shimakawa A, Hines CDG, *et al.* Combination of complex-based and magnitude-based multiecho water-fat separation for accurate quantification of fat-fraction. Magn Reson Med 2011; 66(1): 199-206.
[http://dx.doi.org/10.1002/mrm.22840] [PMID: 21695724]

[21] Mahlke C, Hernando D, Jahn C, *et al.* Quantification of liver proton-density fat fraction in 7.1T preclinical MR systems: Impact of the fitting technique. J Magn Reson Imaging 2016; 44(6): 1425-31.
[http://dx.doi.org/10.1002/jmri.25319] [PMID: 27197806]

[22] Nyquist H. Certain topics in telegraph transmission theory. Trans AIEE 1928; 47(2): 617-44.

[23] Tkác I, Starcuk Z, Choi IY, Gruetter R. *In vivo* 1H NMR spectroscopy of rat brain at 1 ms echo time. Magn Reson Med 1999; 41(4): 649-56.
[http://dx.doi.org/10.1002/(SICI)1522-2594(199904)41:4<649::AID-MRM2>3.0.CO;2-G] [PMID: 10332839]

[24] Zhong X, Nickel MD, Kannengiesser SAR, Dale BM, Kiefer B, Bashir MR. Liver fat quantification using a multi-step adaptive fitting approach with multi-echo GRE imaging. Magn Reson Med 2014; 72(5): 1353-65.
[http://dx.doi.org/10.1002/mrm.25054] [PMID: 24323332]

[25] Hernando D, Hines CDG, Yu H, Reeder SB. Addressing phase errors in fat-water imaging using a mixed magnitude/complex fitting method. Magn Reson Med 2012; 67(3): 638-44.
[http://dx.doi.org/10.1002/mrm.23044] [PMID: 21713978]

[26] Wang X, Hernando D, Reeder SB. Sensitivity of chemical shift-encoded fat quantification to calibration of fat MR spectrum. Magn Reson Med 2016; 75(2): 845-51.
[http://dx.doi.org/10.1002/mrm.25681] [PMID: 25845713]

[27] Fujii M, Shibazaki Y, Wakamatsu K, *et al.* A murine model for non-alcoholic steatohepatitis showing evidence of association between diabetes and hepatocellular carcinoma. Med Mol Morphol 2013; 46(3): 141-52.
[http://dx.doi.org/10.1007/s00795-013-0016-1] [PMID: 23430399]

[28] Reeder SB, Cruite I, Hamilton G. Quantitative assessment of liver fat with magnetic resonance imaging and spectroscopy. J Magn Reson Imaging 2011; 34(4): 729-49.

[29] Ryu JE, Jo W, Choi HJ, *et al.* Evaluation of nonalcoholic fatty liver disease in C57BL/6J mice by using MRI and histopathologic analyses. Comp Med 2015; 65(5): 409-15.
[PMID: 26473344]

[30] Ratziu V, Charlotte F, Heurtier A, *et al.* Sampling variability of liver biopsy in nonalcoholic fatty liver disease. Gastroenterology 2005; 128(7): 1898-906.
[http://dx.doi.org/10.1053/j.gastro.2005.03.084] [PMID: 15940625]

[31] Kang GH, Cruite I, Shiehmorteza M, *et al.* Reproducibility of MRI-determined proton density fat fraction across two different MR scanner platforms. J Magn Reson Imaging 2011; 34(4): 928-34.
[http://dx.doi.org/10.1002/jmri.22701] [PMID: 21769986]

[32] Noureddin M, Lam J, Peterson MR, *et al.* Utility of magnetic resonance imaging *versus* histology for quantifying changes in liver fat in nonalcoholic fatty liver disease trials. Hepatology 2013; 58(6): 1930-40.
[http://dx.doi.org/10.1002/hep.26455] [PMID: 23696515]

[33] Peterson P, Månsson S. Fat quantification using multiecho sequences with bipolar gradients: Investigation of accuracy and noise performance. Magn Reson Med 2014; 71(1): 219-29.
[http://dx.doi.org/10.1002/mrm.24657] [PMID: 23412971]

[34] Haufe WM, Wolfson T, Hooker CA, *et al.* Accuracy of PDFF estimation by magnitude-based and complex-based MRI in children with MR spectroscopy as a reference. J Magn Reson Imaging 2017; 46(6): 1641-7.
[http://dx.doi.org/10.1002/jmri.25699] [PMID: 28323377]

[35] Middleton MS, Haufe W, Hooker J, *et al.* Quantifying Abdominal Adipose Tissue and Thigh Muscle Volume and Hepatic Proton Density Fat Fraction: Repeatability and Accuracy of an MR Imaging–based, Semiautomated Analysis Method. Radiology 2017; 283(2): 438-49.
[http://dx.doi.org/10.1148/radiol.2017160606] [PMID: 28278002]

[36] Insull W Jr. The pathology of atherosclerosis: plaque development and plaque responses to medical treatment. Am J Med 2009; 122(S1): S3-S14.
[http://dx.doi.org/10.1016/j.amjmed.2008.10.013] [PMID: 19110086]